



Original Paper

Characterization of a novel fluidic friction-reduction tool used in extended-reach well considering periodic particle-laden jet



Lu-Bo Tang^a, Xiao-Bin Chen^a, Wei-Wei Xin^b, Shao-He Zhang^{c,d}, Xin-Xin Zhang^{c,d,*}

^a School of Civil Engineering, Central South University, Changsha, 410083, Hunan, China

^b Jiangxi Geological Exploration Bureau for Non-ferrous Metals, Nanchang, 330000, Jiangxi, China

^c Key Laboratory of Metallogenic Prediction of Nonferrous Metals and Geological Environment Monitoring (Central South University), Ministry of Education, Changsha, 410083, Hunan, China

^d School of Geosciences and Info-Physics, Central South University, Changsha, 410083, Hunan, China

ARTICLE INFO

Article history:

Received 13 October 2022

Received in revised form

29 March 2023

Accepted 3 July 2023

Available online 4 July 2023

Edited by Jia-Jia Fei

Keywords:

Extended-reach well

Fluidic oscillator

Vibratory tool

Erosion

Friction reduction

ABSTRACT

Fluidic oscillators (FOs) can be used as an efficient fluidic vibration tool to solve high friction problems in extended-reach wells. However, the complex mechanism of FOs makes the design challenging, and the dynamic erosion behavior inside FOs is still unclear. In this paper, new FOs are proposed and the working characteristics under the influence of periodic particle-laden jets are investigated. Firstly, the results reveal the working mechanism of new FOs, showing that the generation of pressure pulses is closely connected with periodic jet switching and the development of vortices. Secondly, the important performance parameters, i.e., pressure pulse and oscillation frequency, are extensively studied through numerical simulation and experimental verification. It is found that the performance can be optimized by adjusting the tool structure according to different engineering requirements. Finally, the oscillating solid-liquid two-phase flow inside FO is studied. It is demonstrated that the accumulation of particles leads to a significant reduction in performance. The results also reveal five locations that are susceptible to erosion and the erosion behavior of these locations are studied. It has been shown that the periodic jet causes fluctuations in the amount of erosion at the outlet and splitter. This research can provide valuable references for the design and optimization of vibration friction-reduction tools.

© 2023 The Authors. Publishing services by Elsevier B.V. on behalf of KeAi Communications Co. Ltd. This is an open access article under the CC BY-NC-ND license (<http://creativecommons.org/licenses/by-nc-nd/4.0/>).

1. Introduction

Fluidic oscillators (FOs) are served as simple and reliable actuators to generate periodic jet issuing alternatively from two output terminals (Nakayama et al., 2005). Due to the unique nature of jet-switching with no moving parts, FOs have attracted extensive attention and various application versions have been developed (Ghanami and Farhadi, 2019). The wall-attachment-type FO is considered to be the most popular design that is widely applied in engineering practice. Representative applications include measuring (Wright, 1980), mixing (Jeon et al., 2005), sensing (Lee et al., 2002), flow control (Groisman et al., 2003), and enhanced heat transfer (Tesař, 2008). Recently, a relatively new form of applications for FOs is in well drilling processes such as a fluidic

hammer tool for rotary-percussion drilling and a fluidic vibration tool for friction-reduction in extended-reach wells (Peng et al., 2013a; Tang et al., 2021a). These designs usually combine the FOs with a reciprocating piston or a vortex chamber of varying impedance. Fluidic impulse generator (FIG) is a typical fluidic vibration tool that incorporates a piston to produce pressure pulses (Livescu et al., 2017). A reverse-feedback FO with two intersecting feedback loops has been applied to make the automatic switching of the piston motion (Standen and Brunskill, 2012). The application of FIG began to increase in the last decade and achieved good effects in field projects (Hilling et al., 2012). The vortex-controlled variable flow resistance device (VFRD) tool is another representative fluidic vibration tool (Schultz et al., 2012) that introduces a vortex chamber to generate pressure fluctuations. The no-moving-part design greatly improves the performance of the VFRD (Duthie et al., 2017). Currently, these fluidic vibration tools are considered to have more promising prospects (McIntosh et al., 2016). Nevertheless, successful engineering applications are less common than

* Corresponding author.

E-mail address: zhangxx@csu.edu.cn (X.-X. Zhang).

might be expected (Tang et al., 2021a). This may be because the related tools are relatively new, and the complex working mechanism makes the operator circumspect.

FOs have been extensively studied and well-documented in the literature. Livescu and Craig (2018) studied the pressure pulse of FIG through laboratory tests. It is found that the pressure drop depended on the flow rate, tool size, and vibration frequency. Schultz et al. (2012) present the pressure pulse of VFRD. Results show that the pressure waves are similar to the sinusoidal function, which generate gentle force and improve the service life. Further, Shi et al. (2022) make a comprehensive analysis of the working parameters and structural parameters that have obvious effects on the performance of VFRD. Studies of FOs in other fields are relatively common. Through experimental and theoretical analysis, Tesar et al. (2006) reveal complex underlying aerodynamic mechanisms inside a relaxation bistable FO. And it is found that the frequency can be adjusted by the length of the feedback loop. Woszidlo et al. (2014) conduct an experimental study on negative feedback bistatic FO. The results demonstrate that it efficiently reduces the drag of a bluff body. Sarwar et al. (2021) investigate the onset of temporal dynamics of a jet-interaction FO at a low Reynolds number. They point out that the oscillation is mainly driven by pressure momentum that capturing at the exit of the mixing chamber.

Most of the research has focused on single-phase flow behavior within FOs. While a number of studies have noticed the phenomenon of particle erosion and even blocking the internal channels of FOs used in extended-reach-well drilling (Castaneda et al., 2011; Peng et al., 2013b). Few studies have been conducted to investigate the solid-liquid two-phase flow inside the FOs. Meanwhile, the jet-switching process in FOs has made the flow field fairly disordered, and the erosion phenomenon is complicated under dynamic changing state (He et al., 2015).

In this paper, we propose a novel fluidic oscillation tool, named the reverse-feedback fluidic oscillation tool (RFOT), which comprises reverse-feedback channels and vortex chambers. The study reveals the working mechanism of RFOT and analyzes the influence of structural parameters on its performance. Furthermore, multiphase flow simulation is used to investigate the influence of particles on the tool performance and the dynamic erosion behavior.

2. Methodology

In this section, the structure of RFOT is presented. And the experimental device and numerical simulation setup are described.

2.1. Structure of RFOT

Fig. 1(a) shows a schematic diagram of the RFOT. Its size is aimed at the coiled tubing which is commonly used in the extend-reach wells. It consists of a substrate and a cover plate, connected by bolts, and can also be manufactured as a whole using methods such as 3D printing. By inserting the RFOT into an outer tube and connecting them to the drilling tool, a complete axial vibration tool is formed. Fig. 1(b) presents a cross-sectional view of this tool. The upper part is a reverse FO and the bottom part is a vortex chamber. The flow channel includes an inlet, nozzle, control loop, reverse-feedback loop, and outlet. The fluid switches periodically inside the tool to generate pressure pulses. The detailed working mechanism of the tool will be described in the article.

2.2. Experimental setup

As shown in Fig. 2, the experiment devices consist of the upper connector, RFOT, outer tube, bottom connector, pressure sensor (Jiecheng sensor measurement and Control Technology Co., Ltd.,

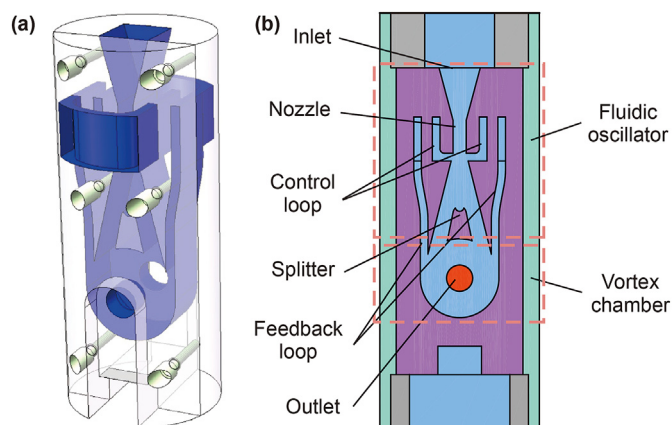


Fig. 1. Schematic of RFOT. (a) 3D model of RFOT, (b) cross-sectional view of RFOT.

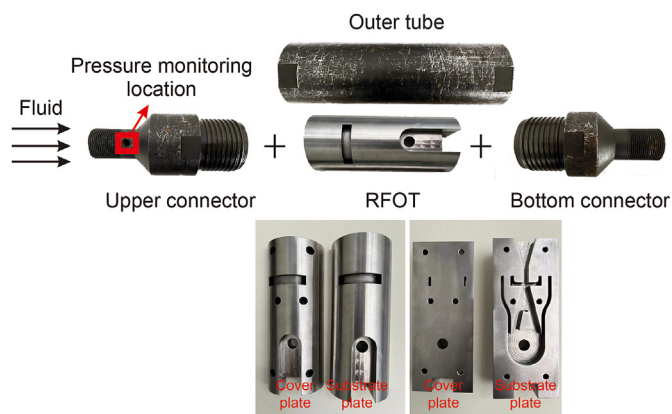


Fig. 2. Schematic diagram of RFOT experiment.

Xi'an, China), and dynamic signal acquisition and analysis system (Donghua Testing Technology Co., Ltd., Jingjiang, China). The RFOT was assembled by bolting the cover plate to the substrate plate. It was inserted into the outer tube which will be connected to the upper and bottom connector by threads.

During the experiment, the fluid is injected from the upper connector by a centrifugal pump. The pressure pulse is monitored at the pressure monitoring location using a pressure sensor with a range of 0–3 MPa and a sampling frequency of 1 kHz. When the pressure pulse is stabilized, the dynamic signal acquisition and analysis system is employed to record the pressure data.

2.3. Methodology of the simulation

Computational fluid dynamics (CFD) method is considered an efficient method to simulate fluid flow due to the feature of precision, intuition, and cost-effectiveness. This technology has been widely used in the numerical simulation of FO and the results are in great agreement with the experimental data (Peng et al., 2013a; Tomac and Hossain, 2020). Besides, CFD is also a powerful tool to predict particle motion by using Lagrangian or Eulerian method (Parsi et al., 2015; Sedrez et al., 2017). For the Eulerian method, particles are considered as a continuous phase which may be problematic in predicting particle behavior close to the wall (Parsi et al., 2014). The Lagrangian method treats particles as a dispersed phase, which allows the forces between the particles to be calculated and makes the results more accurate. Hence, the Lagrangian method was employed.

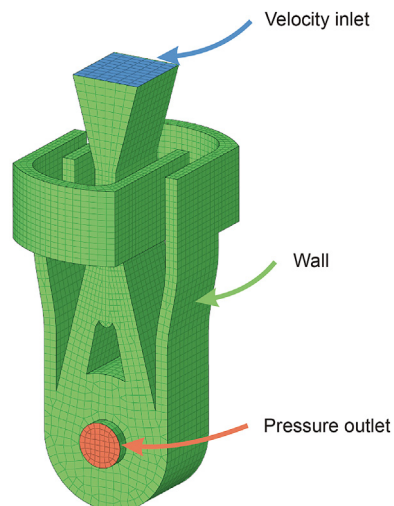


Fig. 3. Typical 3D grid models of the computational domains of RFOT and boundary condition types.

2.4. Computational domains and boundary conditions

The model of the fluid domain of RFOT is shown in Fig. 3. The calculation domain size of RFOT was 42 (X) * 113 (Y) * 58 (Z) mm. Three different mesh densities were calculated, with mesh sizes ranging from 6000 to 25,000. Considering the computational cost and accuracy, the medium density with 12,896 meshes was chosen. As shown in Fig. 3, the velocity inlet boundary was used at the inlet of the nozzle. The pressure outlet boundary was set to atmospheric pressure (the other outlet is not shown due to the viewing angle). In addition, no-slip boundary conditions were used for all wall surfaces.

2.5. Solving strategies

The appropriate time step for simulating FOs has been extensively studied by various researchers, and it has been determined that the time step of 1E-4s is sufficient to achieve the desired level of accuracy while keeping the computational cost reasonable (Peng et al., 2013b; Zhang et al., 2017). The pressure staggered option

(PRESTO) was adopted to calculate pressure. The pressure implicit split operator (PISO) algorithm was used to deal with the coupled velocity and pressure problem. In addition, the quadratic upstream interpolation for the convective kinetics (QUICK) scheme was employed for momentum equations, turbulent kinetic energy, and turbulent dissipation rate.

2.6. Turbulence model

The turbulence phenomenon is common in RFOT, hence the choice of a suitable turbulence model is important for calculation accuracy (Peng et al., 2013a). The common turbulence models used in simulations of FOs are the standard $\kappa-\epsilon$ turbulence model, the RNG-based model, and the realizable $\kappa-\epsilon$ model (Olsen et al., 2017; Peng et al., 2013a). A comparison of numerical simulations using different turbulence models with experiments was conducted. As shown in Fig. 4, the minimum pressure drop obtained by the standard $\kappa-\epsilon$ model is close to the experimental results, nevertheless, the obtained maximum pressure drop shows a relatively pronounced deviation. The RNG model exhibits some difference when calculating minimum pressure drop. The pressure drop obtained from the realizable $\kappa-\epsilon$ model is in great agreement with the experimental value. To obtain the accurate oscillation frequency, the time-pressure data is processed by the fast Fourier transform (FFT), and the horizontal coordinate of the first peak is the desired value (Tesar and Jilek, 2013). The oscillation frequency obtained through the experiment is 12.21 Hz. The frequency calculated by the realizable $\kappa-\epsilon$ model, standard $\kappa-\epsilon$ turbulence model, and RNG-based model is 12.01, 10.01, 14.02 Hz respectively. Therefore, the realizable $\kappa-\epsilon$ model provided the most accurate pressure and frequency results and it was adopted in the following simulations of this paper.

2.7. Erosion model and particle-wall rebound model

The erosion model and rebound model are essential to accurately simulate erosion behavior (Parsi et al., 2014). The erosion model can obtain the amount of erosion caused by the particles. And the rebound model can simulate the rebound angle and velocity of particles when they impact the target wall. To select suitable erosion models and rebound models for fluidic oscillator simulation, Tang et al. (2021b) compared different models with

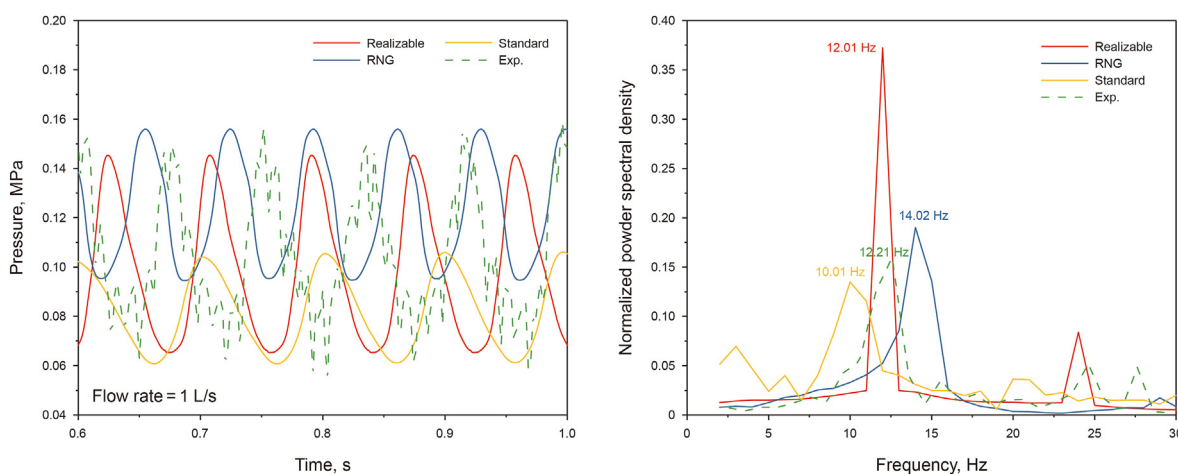


Fig. 4. The pressure and frequency obtained by experiments and simulations using different turbulence models.

Table 1
 Numeric parameters and boundary conditions.

Information	Adopted condition
Erosion model	Oka erosion model
Particle impact and rebound model	Grant and Tabakoff model
Multiphase model	Euler-Lagrangian
Turbulence model	Realizable $k-\epsilon$
Average time-step	1E-4 s
Scheme of velocity-pressure coupling	PISO
Spatial discretization for pressure	PRESTO
Inlet	Velocity inlet
Outlet	Pressure outlet
Discretization scheme for momentum equation, kinetic energy equation, and turbulence dissipation rate equation	QUICK

experimental results. The results demonstrated that the OKA erosion model (Oka et al., 2005) with the Grant and Tabakoff particle-wall rebound model (Grant and Tabakoff, 1975) worked best, and the two models will be used in the simulation of this paper.

The Oka erosion model in CFD is expressed as

$$E = E_{90} \left(\frac{V}{V_{ref}} \right)^{k_2} \left(\frac{d}{d_{ref}} \right)^{k_3} f(\gamma) \quad (1)$$

$$f(\gamma) = (\sin \gamma)^{n_1} [1 + Hv(1 - \sin \gamma)]^{n_2} \quad (2)$$

where E_{90} is the reference erosion ratio, d and d_{ref} are the particle diameter (mm) and particle reference diameter (mm), V is the particle impact velocity (m/s), V_{ref} is the reference velocity (m/s), k_2 and k_3 are the velocity and diameter exponents, $f(\gamma)$ is the impact angle function, and n_1 and n_2 are exponents determined by the material hardness and other impact conditions, Hv is the vickers hardness number (GPa).

The model proposed by Grant and Tabakoff is given by

$$e_n = 0.993 - 0.0307\theta + 4.75 \times 10^{-4}\theta^2 - 2.61 \times 10^{-6}\theta^3 \quad (3)$$

$$e_t = 0.988 - 0.0289\theta + 6.43 \times 10^{-4}\theta^2 - 3.56 \times 10^{-6}\theta^3 \quad (4)$$

where e_n and e_t are the restitution coefficients for normal and tangential velocity components, and θ is the particle incidence radian. Besides, the main characteristics of the simulations are shown in Table 1.

3. Working mechanism of reverse-feedback fluidic oscillator tools

The structure of RFOT may be deceptively simple. However, the working mechanism is quite complex which consists of the wall attachments, jet turbulence, and secondary vortices. According to the Coanda effect (Coanda, 1936), the fluid entering the fluidic oscillator is randomly attached to one of the output channels. When the speed of the fluid in the vortex chamber is slow, the fluid flows towards the outlet and the pressure drop of RFOT is low (point a in Fig. 5). As the main jet develops in the vortex chamber, the velocity and the centrifugal force of the fluid increase, making it difficult for the fluid to flow out from the outlet. Hence, the tool pressure continues to rise (point b in Fig. 5). Meanwhile, a portion of the main jet flows into the feedback channel which subsequently flows through the control channel and pushes against the main jet. When the critical value is reached, the main jet deflects to the other

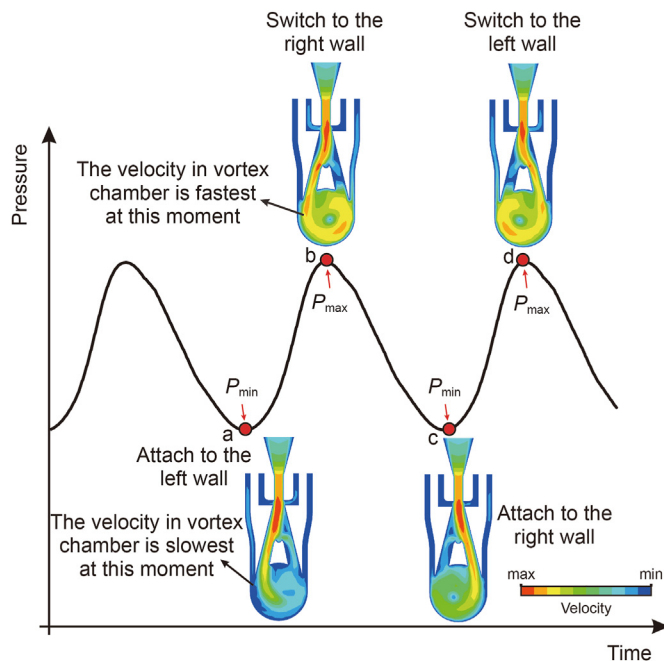


Fig. 5. Pressure pulse generated by RFOT and the corresponding switching process.

side (point c in Fig. 5). At this point, half of the switching process is completed and the rest of the process will be completed in the same way (point d in Fig. 5). Fig. 6 shows the velocity streamlines of the RFOT. Fig. 6(i) presents the moment when the fluid is attached to the left side. A trapped vortex above the splitter and a blocking vortex in the right output channel prevents the main jet from flowing into the right output channel and enhances the attachment of the main jet. Thus, most of the fluid flows into the left output channel which weakens the interaction between the fluid of the two output channels. As a result, the trapped vortex and blocking vortex gradually disappear (as shown in Fig. 6(ii)). With the development of the jet in the vortex chamber, fluid flows back to the left control loop and applies momentum to the main jet, the jet begins to switch to the right. The trapped vortex appears again and has an obstructive effect on the jet switching (as shown in Fig. 6(iii)). As the jet switching proceeds, the trapped vortex is destroyed and a separated vortex begins to appear on the left side which contributes to the jet switching (as shown in Fig. 6(iv)). And a blocking vortex then appears in the left output channel and prevents the jet from flowing into the left output channel (as shown in Fig. 6(v)). This vortex also contributes to the switching of the jet and the jet is finally switched to the right side (as shown in Fig. 6(v) and (vi)).

During the process of research, the RFOT tool was found to exhibit a slightly higher oscillation frequency (as shown in Fig. 4). To meet the different working conditions, the RFOT was optimized by adding two vortex chambers and dividing it into a two-outlet version and a six-outlet version. As shown in Fig. 7(a) and (b), they were called multiple chambers reverse-feedback fluidic oscillation tools (MRFOT). The calculation domain size of MRFOT was 50 (X) * 224 (Y) * 58 (Z) mm.

4. Results and discussion

4.1. Performance analysis

The fluidic vibration tool is designed to generate pressure pulses

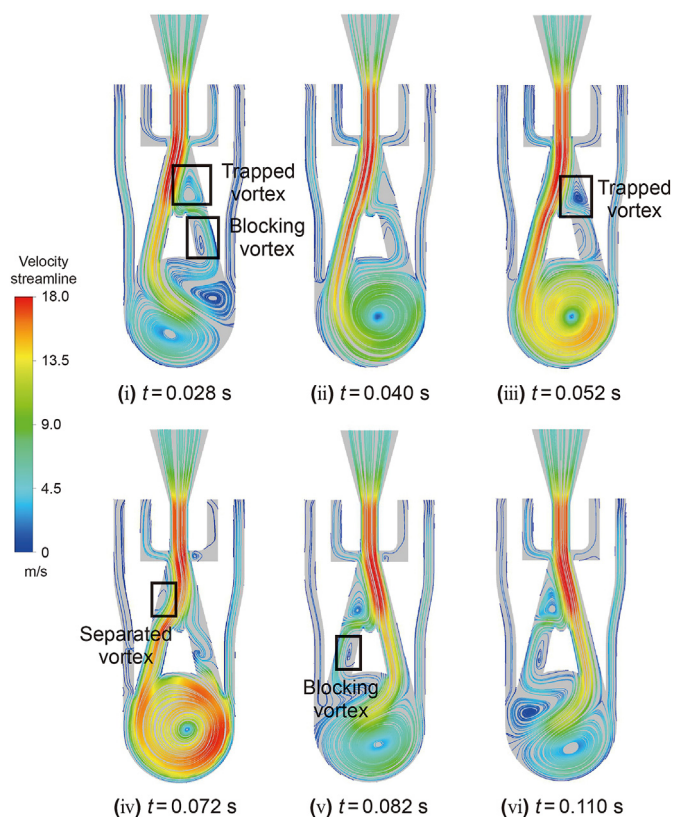


Fig. 6. The streamline of the flow field in RFOT.

that vibrate the drill pipe and reduce friction. The friction-reduction performance is mainly determined by the pressure pulse amplitude, the average pressure drop, and the oscillation frequency of the FO. In this section, we will discuss the performance of tools with different fluid parameters and explore the effect of different structural parameters on performance.

4.1.1. Effect of flow rate on performance

The effects of flow rates, i.e., 1, 1.5, 2, 4, 6, and 8 L/s, on average pressure drop, pressure pulse amplitude, and oscillation frequency were studied. As shown in Fig. 8, the average pressure drop and pressure pulse amplitude of the three tools varies exponentially with the flow rate. At the flow rate of 1 L/s, the pressure pulse amplitude of RFOT, six-outlet version MRFOT, and two-outlet version MRFOT are 0.081, 0.035, and 0.103 MPa. And the average pressure drop of the three tools is 0.097, 0.084, and 0.143 MPa, respectively. When the flow rate is 8 L/s, the pressure pulse amplitude of the three tools is 5.327, 2.732, and 7.011 MPa, and the average pressure drop is 6.378, 5.618, and 8.809 MPa, respectively. It was observed that the average pressure drop and pressure pulse amplitude of the two-outlet version MRFOT are the largest. This is because as the number of vortex chambers increases, the fluid is accelerated to a higher velocity which makes the pressure drop higher. The pressure pulse of MRFOT with six outlets is the smallest. The reason is that the increase of outlets makes more fluid flow away which reduces fluid velocity and pressure drop.

As shown in Fig. 9, the frequency of the three tools is proportional to the flow rate. The oscillation frequency of RFOT is higher than that of MRFOT. Take the six-outlet version MRFOT as an example to illustrate the mechanism for reducing the frequency. As shown in Fig. 10, process (i) and process (ii) are similar to RFOT. The velocity of the fluid is increasing and the direction of the fluid in the

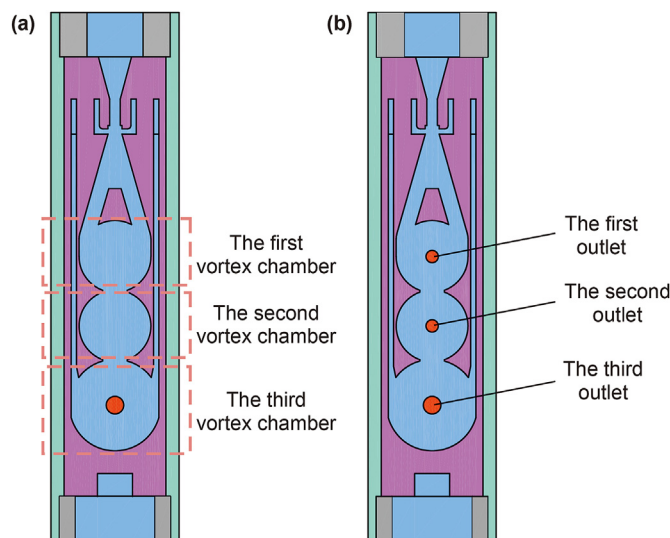


Fig. 7. Schematic of MRFOT. (a) MRFOT with two outlets, (b) MRFOT with six outlets.

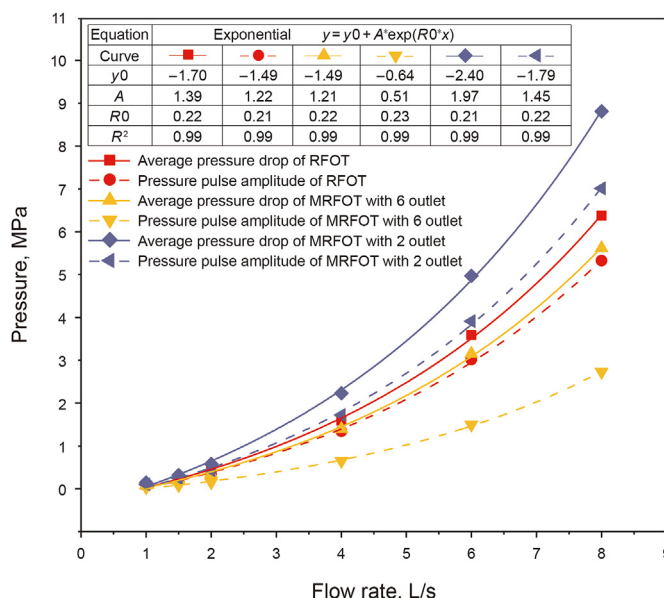


Fig. 8. Effect of flow rate on average pressure drop and pressure pulse amplitude.

third vortex chamber is counterclockwise. However, as shown in process (iii), when the main jet switches to the other side, the direction remains counterclockwise. And the direction changes clockwise after it develops for some time (shown in process (iv) and process (v)). The delay of the fluid in the third vortex chamber hinders the flow of the upper fluid and reduces the switching sensitivity. In addition, as the length of the feedback channel becomes longer, the time for the fluid to return to the control channel becomes longer, which also increases the time of the switching process.

To ensure the accuracy of the numerical simulations, experimental tests were performed. Fig. 11 displays the frequency data obtained from both the experiment and the simulation, which shows a high level of agreement. The pressure drop obtained from the experiment and CFD simulation is consistent when the flow rate is low. Some error exists when the flow rate increases which may be attributed to the low manufactured accuracy of the RFOT.

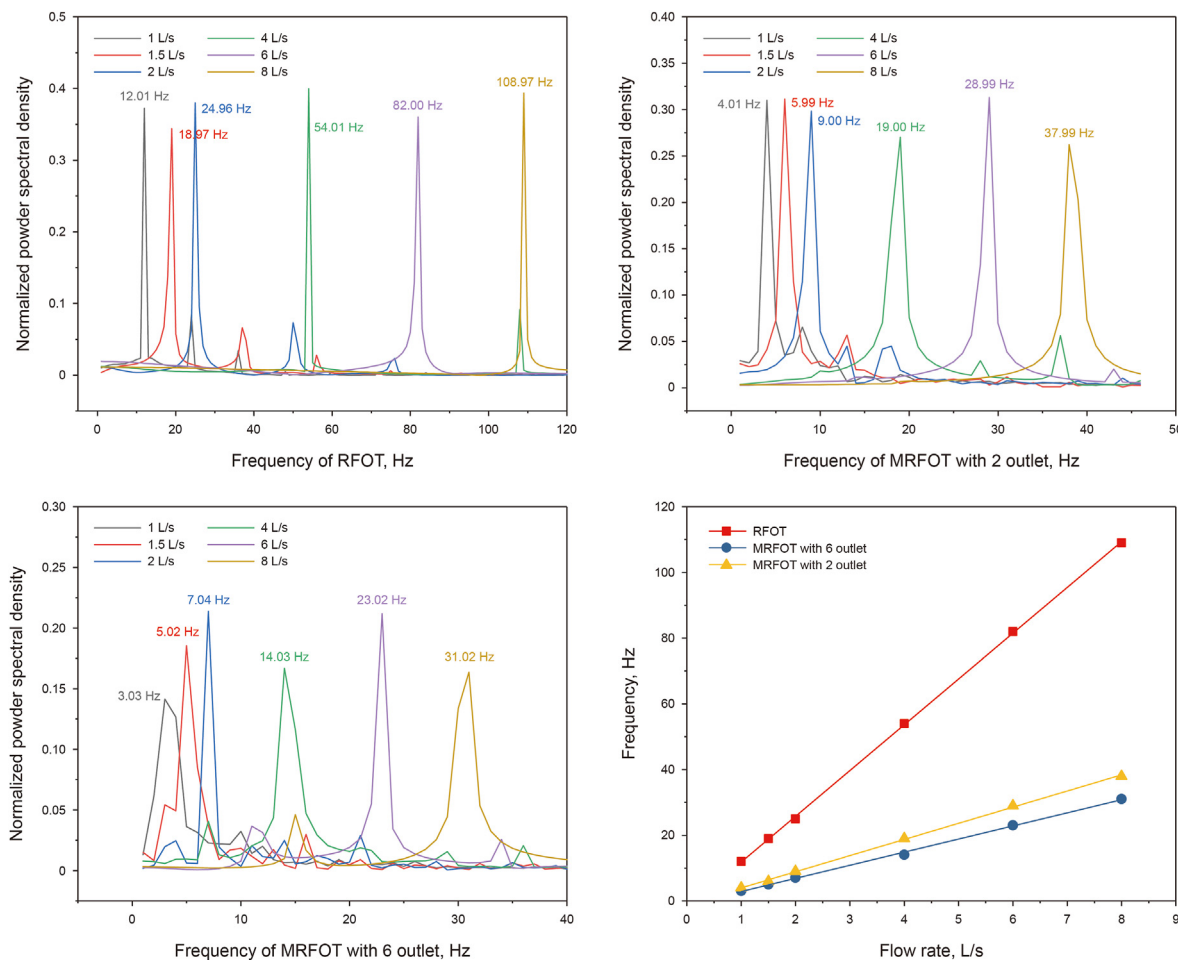


Fig. 9. Effect of flow rate on frequency.

Specifically, due to the asymmetry of the tool, the jet tends to switch before it fully attaches to one output channel, leading to collisions and generating higher pressure.

4.1.2. Effect of structural parameters on the performance

The structural parameters of the FOs have a significant effect on the performance. The important structural parameters are outlet size, nozzle-to-splitter distance, and channel depth. In this section, a flow rate of 2 L/s was used to explore the effect of structural parameters on the performance of RFOT. The outlet size of 8, 10, 12, 14, and 16 mm, the nozzle-to-splitter distance of 24, 25, 26, 27, and 28 mm, and the channel depth of 18, 19, 20, 21, and 22 mm were adopted.

As shown in Fig. 12, the pressure pulse amplitude decreases linearly from 0.48 to 0.19 MPa with the increase in outlet size. The average pressure and frequency show an exponential decrease. It can also be observed that the average pressure drop decreases at a decreasing rate. The reason is that as the outlet size increases, the flow space in the vortex chamber becomes small, making it easier to form high-speed vortices, which slows down the decreasing rate of the pressure drop. The frequency decreases at an increasing rate. This is because as the outlet size increases, less fluid flows back to the control port, and the momentum applied to the main jet becomes small.

As shown in Fig. 13, the average pressure drop and pressure pulse amplitude increase with the increase of nozzle-to-splitter distance. This is due to that the large nozzle-to-splitter distance is more favorable for the development of the high-speed jet. It is

observed that the oscillation frequency reduces from 26 to 20.4 Hz. This is caused by the increase in flow distance. The effect of flow channel depth on the pressure pulse and frequency was also investigated and found to have no significant effect within a certain range. The FO performance can be optimized by adjusting the tool structure to meet complex engineering requirements. The pressure can be reduced by increasing the outlet size and reducing the nozzle-to-splitter distance, and the oscillation frequency can be reduced by increasing the outlet size and the nozzle-to-splitter distance.

4.1.3. Effect of particle parameters on the performance

As the solids control system can not completely remove particles from the drilling fluid, it is necessary to study the effect of particles on performance. Fig. 14(a) shows the effect of flow rate on the performance when taking into account the effect of particles. The solid content is 0.005, and the particle size is 2 μm. It is demonstrated that the three performance parameters are significantly reduced by the addition of particles. This is because the accumulation of particles impedes the flow of the fluid (shown in Fig. 14(d)). As the flow rate increases, the accumulation of particles is decreased and improves the tool's performance. Fig. 14(b) shows the effect of particle size. The selected solid content is 0.005, and the flow rate is 4 L/s. When the particle size is in the range of 2–8 μm, the pressure pulse and frequency decrease at a faster rate. While the effect of particles is negligible as the particle size continues to increase. This is due to the fact that smaller particles tend

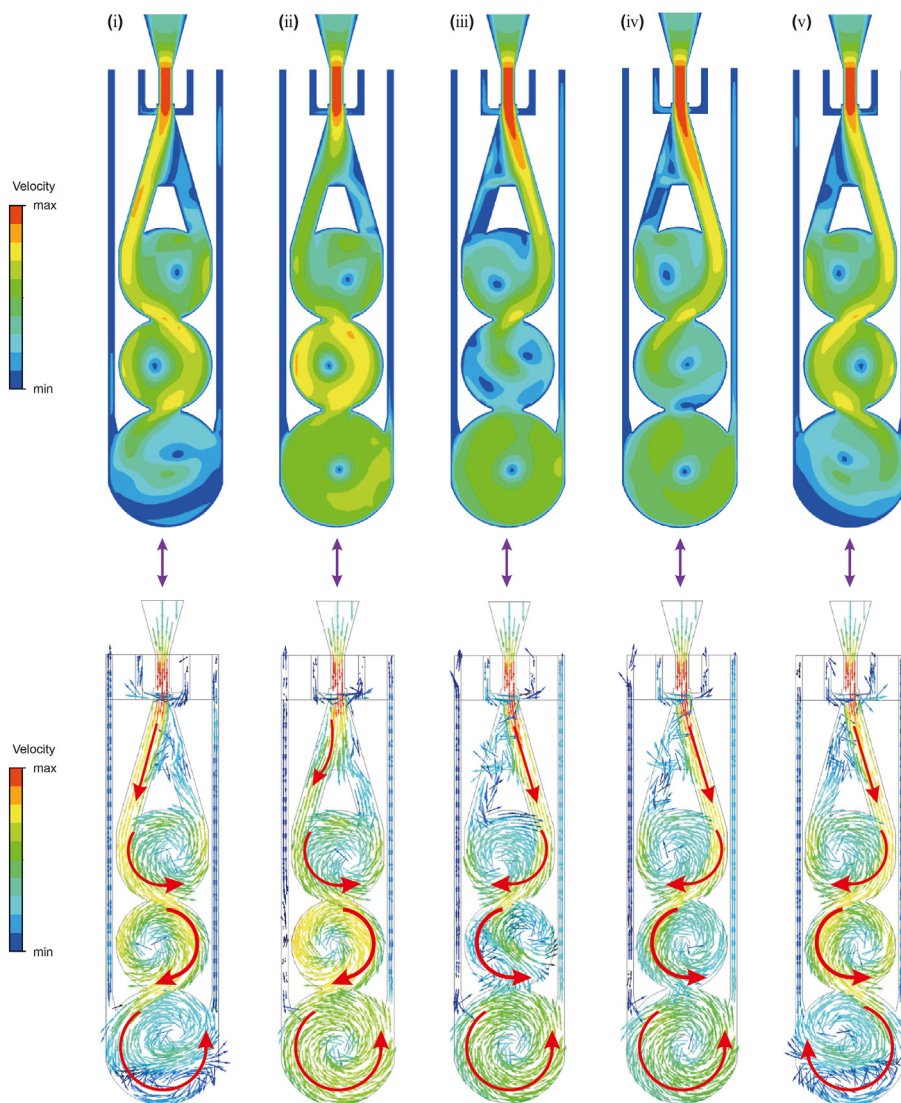


Fig. 10. Typical instances of fluid flow and the jet-switching process in a MRFOT with six outlets.

to accumulate in the corners, and the larger diameter particles are more easily carried away by the drilling fluid. Fig. 14(c) shows the effect of solid content. Particle size is 2 μm and the flow rate is 4 L/s. Because the increase of solid phase content corresponds to the numerical simulation for a small-size FO. Hence, the frequency and average pressure pulse increase with the increasing solid content, while the pressure pulse amplitude decreases.

4.2. Erosion analysis of RFOT

The high-speed drilling fluid loaded with solid particles is prone to cause erosion phenomena in the FO. And the FO is a delicate component and can fail easily once it is eroded. To prevent this from happening, erosion analysis is conducted.

Using the CFD method, the behavior of particles is simulated by the Lagrangian approach and that of fluid is simulated by the Eulerian approach (Kosinski and Hoffmann, 2009; Pereira et al., 2014). The simulation results show that the location of maximum erosion mainly occurs in five places, i.e., splitter, outlet, bottom, nozzle, and control port (shown in Fig. 15). In this section, the effect of fluid parameters, particle parameters, and jet switching on erosion behavior will be investigated.

4.2.1. Effect of volume flow rate on erosion behavior

The flow rate of 2, 4, 6, and 8 L/s was adopted, the particle diameter was 2 μm and the solid content of the particle was 0.5%. As shown in Fig. 16, the erosion amount at each location increases exponentially as the flow rate increases. It can be explained by the fact that as the flow velocity increases, the momentum of the particles also increases, leading to more severe impact on the target wall. The maximum erosion position occurs at the control port and the minimum is at the bottom.

4.2.2. Effect of particle size on erosion behavior

Six cases with different particle sizes were studied. Particle sizes of 2, 4, 6, 8, 20, and 40 μm were adopted, and the flow rate and solid content are 4 L/s and 0.5%, respectively. The simulation results are shown in Fig. 17. It can be observed that the amount of erosion at the nozzle first increases and then decreases. This is a common phenomenon in the field of erosion. As the particle size increases, the kinetic energy of the particles increases, and the erosion becomes severe. When the particle size increases to a certain extent, the carrying effect of fluid on the particle is weakened. Hence the particle velocity decrease and reduce erosion.

It is shown that the erosion in the control port decreases rapidly

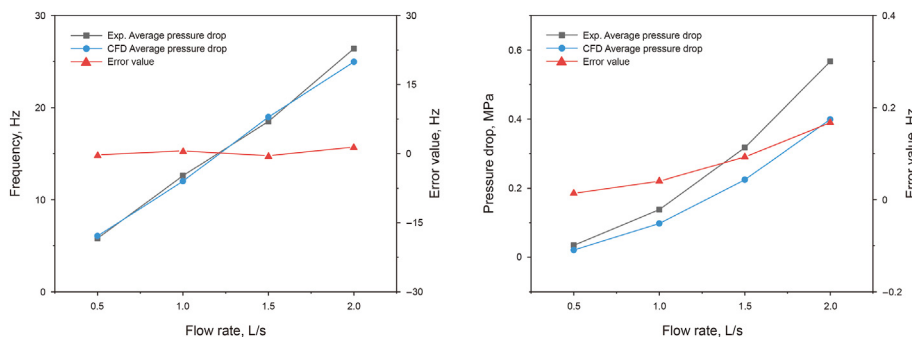


Fig. 11. Verification of frequency and pressure drop obtained from experiments and CFD simulations.

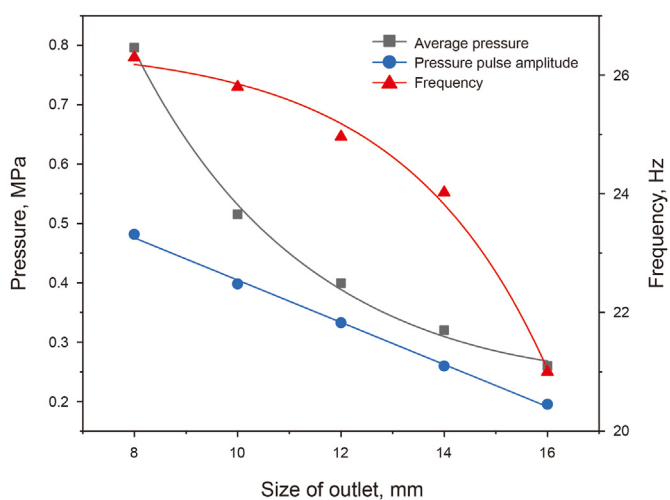


Fig. 12. Effect of size of outlet on performance.

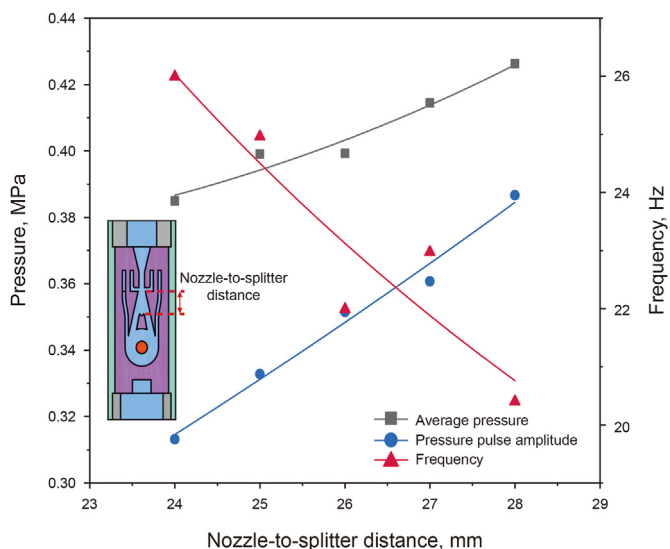


Fig. 13. Effect of nozzle-to-splitter distance on performance.

when particle diameters are between 2 and 6 μm , after which it tends to stabilize. This is also due to the carrying effect of fluid on the particle. When the particle diameter is small, the fluid has strong carrying effects on the particle. As the jet keeps switching between the two output channels (as shown in Fig. 5), small

particles are driven to impact the control port thus causing larger erosion. However, as the particle diameter increase, the carrying effect of the fluid on the particles diminishes. Most of the particles move directly downward rather than impact control ports.

The erosion curve of the splitter is unusual, which shows a trend of first decreasing and then increasing. This is attributed to the concave shape of the splitter which accumulates many particles in the vicinity (shown in Fig. 18). These particles prevent other particles from impacting the splitter. As the particle size increases, the number of accumulated particles increases, and the amount of erosion decreases. When the particle size becomes large, it becomes difficult for the particles to accumulate here, thus the erosion becomes severe.

For the outlet and bottom, the erosion amount always increases with the increase of particle size. This is because the velocity at these locations is higher and the increase in particle size does not significantly affect the carrying effect of the fluid on the particles. And it can also be observed that the maximum erosion position changes from the control port to the outlet when the particle size is greater than 2.28 μm .

4.2.3. Effect of solid content on erosion characteristics

The solid content of 0.5%, 1%, 1.5%, 2%, 2.5%, and 5% was used. The particle size is 2 μm and the flow rate is 4 L/s. As shown in Fig. 19, all positions except for the splitter vary linearly with solid content. This is because the particle number increases linearly with the increase of solid content for a given particle size. The frequency of impacting on the target wall increase and the erosion becomes severe. It can be found that the erosion velocity of the splitter first increases, then decreases, and finally even approaches 0 m/s. This is due to particle accumulation caused by the concave splitter. When the solid content is low, few particles accumulated in the splitter. It is not enough to form protection for the splitter and the erosion speed increase. When the solid phase content is large to a certain value, the protection for the splitter is obvious and leads to a significant reduction of the erosion speed.

When the solid phase content range from 0.85% to 4.37%, the maximum erosion position occurs at the splitter, and the rest of the time, it occurs at the control port. In addition, the erosion behavior of the splitter, nozzles, and control port are all sensitive to the solid phase content.

4.2.4. Effect of periodic oscillation on erosion characteristics

FOs are characterized by periodic switching of the jet, and the study of the erosion behavior caused by dynamic jets is innovative. A group of cases with the particle size of 2 μm , the flow rate of 4 L/s, and the solid phase content of 0.5% are selected. As shown in Fig. 20, the amount of erosion over time was monitored.

As can be seen from Fig. 20, the amount of erosion at the nozzle

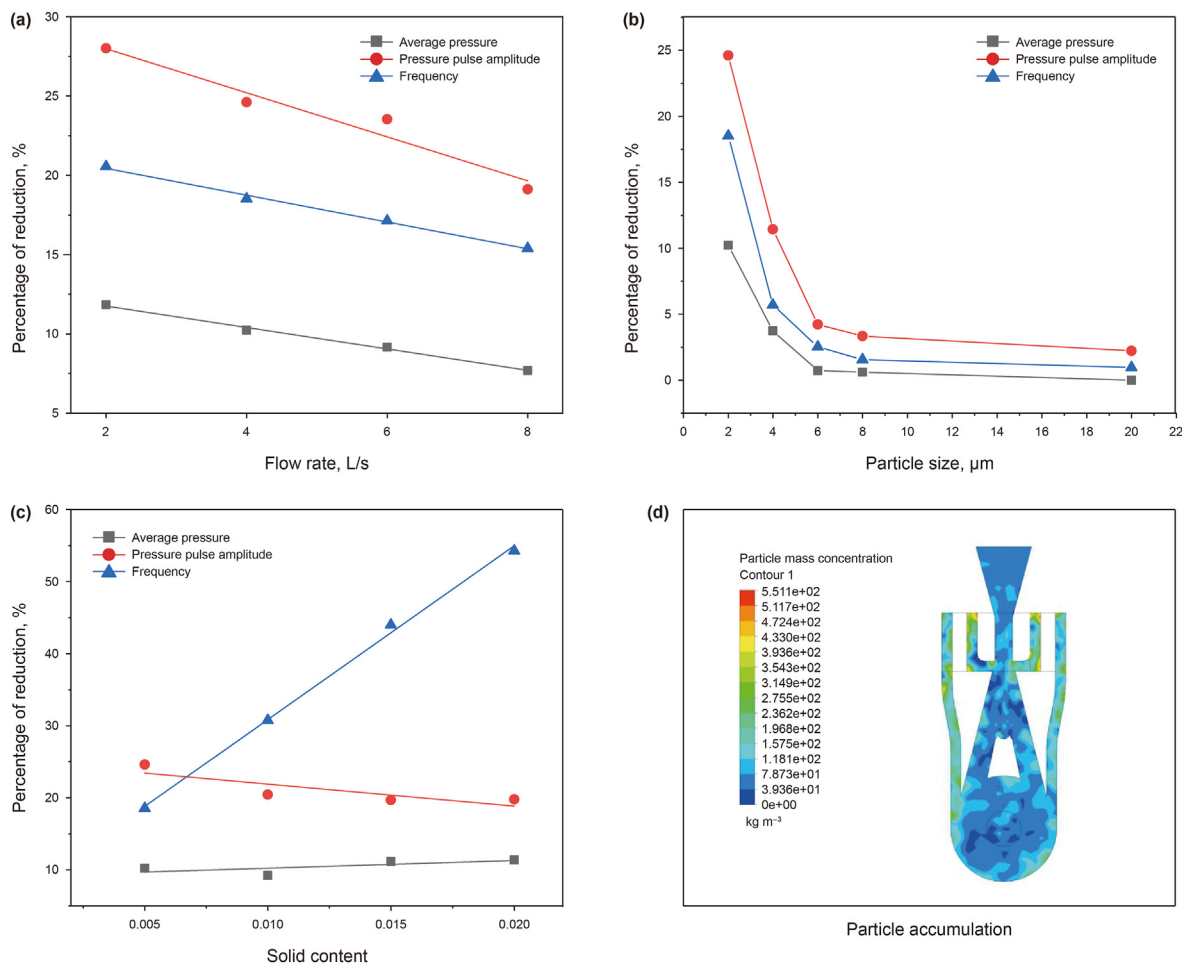


Fig. 14. Effect of particle parameters on performance and the schematic of particle accumulation in FO.

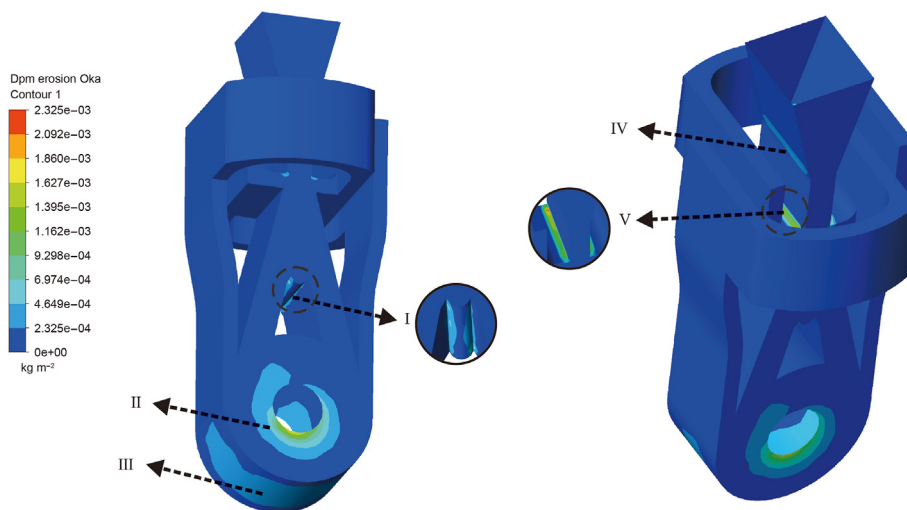


Fig. 15. The location where RFOT is most susceptible to erosion.

increases linearly because the impact of the particles on the nozzle is continuous. The erosion curve at the bottom shows only slight fluctuations because the bottom is affected by particle-laden fluid most of the time. The amount of erosion in the outlet and splitter

shows a periodic increase, with each cycle increasing and then leveling off. This is because when the particle-laden fluid impacts the target wall, the amount of erosion rises, and when the fluid switches to the other side, the erosion volume will remain stable.

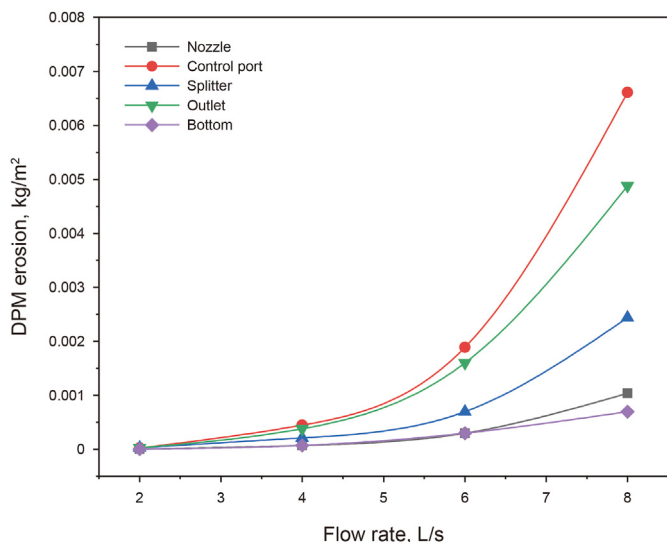


Fig. 16. Effect of flow rate on erosion.

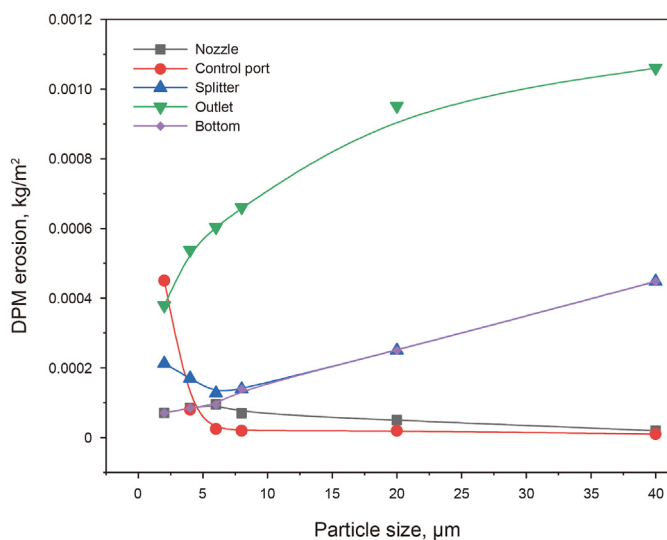


Fig. 17. Effect of particle size on erosion.

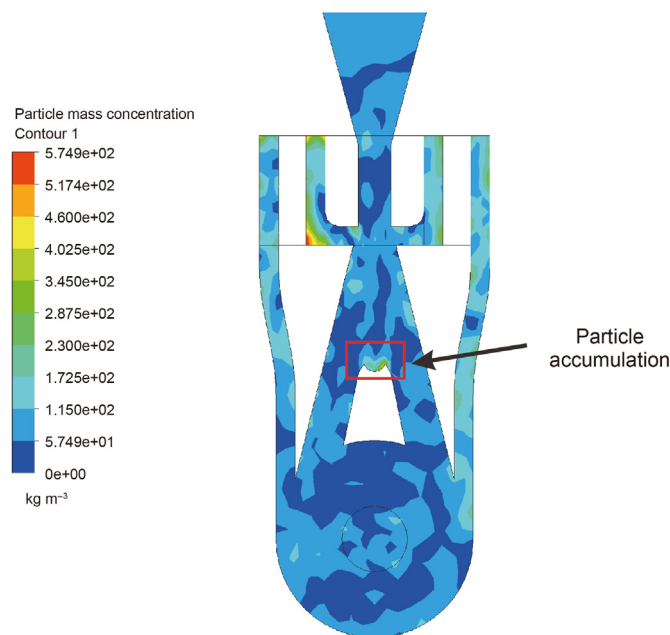


Fig. 18. Particle accumulation occurred in the vicinity of the splitter.

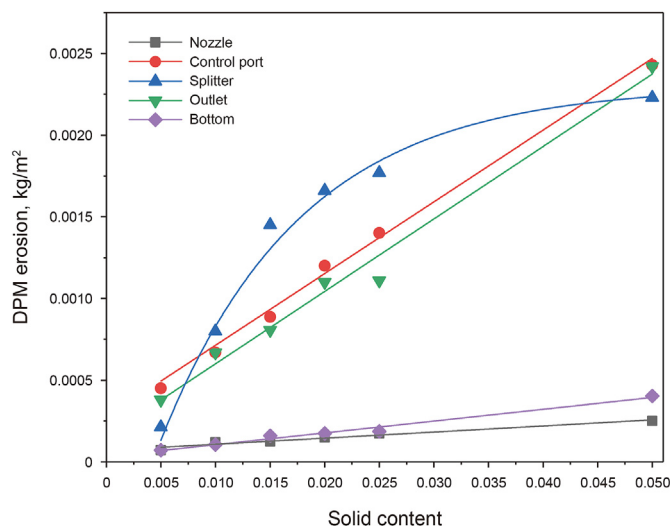


Fig. 19. Effect of solid content on erosion.

It can be observed that one fluctuation period of the outlet curve is exactly equal to the oscillation period of RFOT, while one fluctuation period of the splitter is twice the oscillation period. The reason for this difference is that the outlet is exposed to erosion during each vibration period, while one side of the splitter is only exposed once during two vibration periods (as shown in Fig. 5).

5. Conclusions

New reverse-feedback FOs used as fluidic vibration tools were presented. The no-moving-part design reduces the length of the tool, increases the build-up rate, and exhibits resistance to extremely harsh environments. Through CFD simulation and experimental verification, the conclusions are as follows:

The mechanism of generating the pressure pulse of RFOT was revealed, which is closely related to jet switching and the development of the vortex. The effect of flow rate and structure parameters on pressure pulse and oscillation frequency was investigated. Results show that as the outlet size increases, the

average pressure drop decreases at a decreasing rate while the oscillation frequency decreases at an increasing rate. The increase of nozzle-to-splitter distance increases the pressure pulse and reduces the oscillation frequency.

The effects of particles were considered, and it was found that particles blocked the flow channels and lead to a significant reduction in tool performance. And the particles are prone to erode the nozzle, splitter, control port, outlet, and bottom of the tool. The increase in solid content causes particles to accumulate at the splitter, resulting in a trend of increasing and then decreasing erosion rate. The particle size and solid content affect the erosion behavior by altering the particle accumulation and the carrying effect of fluid on particles. Dynamic erosion characteristics under the influence of periodic jets were revealed, and the amount of erosion in the splitter and outlet increased in a fluctuating manner.

One of the challenges to design FOs is determining the structure

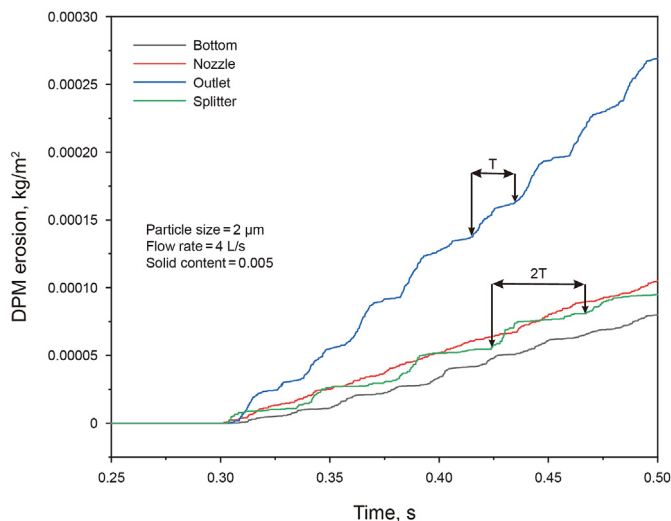


Fig. 20. Dynamic erosion behavior in the RFOT.

parameters that can enable jets to switch and generate periodic pressure pulses. Current literature shows that designers rely heavily on their experience in determining these parameters, often leading to time-consuming trial-and-error processes that increase costs. In future research, we plan to train machine learning models which can make precise predictions to assist designers in effectively designing FOs. Meanwhile, the rheological property of the drilling fluid has great effects on the tool performance. Therefore, we also plan to consider the effects of the rheological constitutive model and time-dependent viscosity characteristics on FO performance in subsequent studies.

Declaration of competing interest

The authors declare that they have no known competing financial interests or personal relationships that could have appeared to influence the work reported in this paper.

Acknowledgments

This research was funded by the National Key Research and Development Program of China under grant number 2020YFC1807200; the National Natural Science Foundation of China under grant number 41872186; the National Natural Science Foundation of China (Grant number 51978674)

Nomenclature

FOs	Fluidic oscillators
FIG	Fluidic impulse generator
VFRD	Vortex-controlled variable flow resistance device
RFOT	Reverse-feedback fluidic oscillation tool
MRFOT	Multiple chambers reverse-feedback fluidic oscillation tools
CFD	Computational fluid dynamics
FFT	Fast Fourier transform
PRESTO	Pressure staggered option
PISO	Pressure implicit split operator
QUICK	Quadratic upstream interpolation for convective kinetics

References

- Castaneda, J.C., Schneider, C.E., Brunskill, D., 2011. Coiled tubing milling operations: successful application of an innovative variable water hammer extended-reach BHA to improve end load efficiencies of a PDM in horizontal wells. In: SPE/ICoTA Coiled Tubing & Well Intervention Conference and Exhibition, the Woodlands, Texas, USA, 5–6 April. <https://doi.org/10.2118/143346-MS>.
- Coanda, H., 1936. Device for Deflecting a Stream of Elastic Fluid Projected into an Elastic Fluid. US Patent, 2052869.
- Duthie, L., Namlah, S., Abdulghani, A., et al., 2017. Mega reach case study, Saudi Arabia; the application of fluidic oscillation vibratory tools in tackling a challenging coiled tubing well intervention. In: SPE/ICoTA Well Intervention and Coiled Tubing Conference and Exhibition, the Woodlands, Texas, USA, 21–22 March. <https://doi.org/10.2118/184770-MS>.
- Ghanami, S., Farhadi, M., 2019. Fluidic oscillators' applications, structures and mechanisms-A review. *Trans. Phenom. Nano Micro Scales* 7 (1), 9–27. <https://doi.org/10.22111/tpnms.2018.25051.1153>.
- Grant, G., Tabakoff, W., 1975. Erosion prediction in turbomachinery resulting from environmental solid particles. *J. Aircraft* 12, 471–478. <https://doi.org/10.2514/3.59826>.
- Groisman, A., Enzelberger, M., Quake, S.R., 2003. Microfluidic memory and control devices. *Science* 300 (5621), 955–958. <https://doi.org/10.1126/science.1083694>.
- He, J., Zhang, P., Yin, Q., Yin, K., et al., 2015. Study of drilling muds on the anti-erosion property of a fluidic amplifier in directional drilling. *Fracture and Structural Integrity* 9 (34), 564–573. <https://doi.org/10.3221/IGF-ESIS.34.62>.
- Hilling, S., Ayling, G., Yeung, J., 2012. Optimizing coil tubing extended-reach capabilities through application of downhole friction reduction tools. In: SPE/ICoTA Well Intervention and Coiled Tubing Conference and Exhibition, the Woodlands, Texas, USA, 27–28 March. <https://doi.org/10.2118/154290-MS>.
- Jeon, M.K., Kim, J., Noh, J., 2005. Design and characterization of a passive recycle micromixer. *J. Micromech. Microeng.* 15, 346–350. <https://doi.org/10.1088/0960-1317/15/2/014>.
- Kosinski, P., Hoffmann, A.C., 2009. Extension of the hard-sphere particle-wall collision model to account for particle deposition. *Phys. Rev. E* 79 (6), 061302. <https://doi.org/10.1103/PhysRevE.79.061302>.
- Lee, G., Kuo, T., Wu, W., 2002. A novel micromachined flow sensor using periodic flapping motion of a planar jet impinging on a V-shaped plate. *Exp. Therm. Fluid Sci.* 26 (5), 435–444. [https://doi.org/10.1016/S0894-1777\(02\)00155-3](https://doi.org/10.1016/S0894-1777(02)00155-3).
- Livescu, S., Craig, S.H., 2018. A critical review of the coiled tubing friction-reducing technologies in extended-reach wells. Part 2: vibratory tools and tractors. *J. Pet. Sci. Eng.* 166, 44–54. <https://doi.org/10.1016/j.petrol.2018.03.026>.
- Livescu, S., Craig, S., Aitken, B., 2017. Fluid-hammer effects on coiled-tubing friction in extended-reach wells. *SPE J.* 22 (1), 365–373. <https://doi.org/10.2118/179100-PA>.
- McIntosh, T., Baros, K.J., Gervais, J.G., 2016. A vibratory tool study on extended reach horizontals during coiled tubing drillout in the eagle ford shale. In: SPE/ICoTA Well Intervention and Coiled Tubing Conference and Exhibition, Houston, Texas, USA, 22–23 March. <https://doi.org/10.2118/179087-MS>.
- Nakayama, A., Kuwahara, F., Kamiya, Y., 2005. A two-dimensional numerical procedure for a three dimensional internal flow through a complex passage with a small depth (its application to numerical analysis of fluidic oscillators). *Int. J. Numer. Methods Heat Fluid Flow* 15, 863–871. <https://doi.org/10.1108/09615530510625129>.
- Oka, Y., Okamura, K., Yoshida, T., 2005. Practical estimation of erosion damage caused by solid particle impact: Part 1: effects of impact parameters on a predictive equation. *Wear* 259 (1), 95–101. <https://doi.org/10.1016/j.wear.2005.01.039>.
- Olsen, J.J., Hemmingsen, C.S., Bergmann, L., et al., 2017. Characterization and erosion modeling of a nozzle-based inflow-control device. *SPE Drill. Complet.* 32 (4), 224–233.
- Parsi, M., Agrawal, M., Srinivasan, V., et al., 2015. CFD simulation of sand particle erosion in gas-dominant multiphase flow. *J. Nat. Gas Sci. Eng.* 27, 706–718. <https://doi.org/10.1016/j.jngse.2015.09.003>.
- Parsi, M., Najmi, K., Najjafard, F., et al., 2014. A comprehensive review of solid particle erosion modeling for oil and gas wells and pipelines applications. *J. Nat. Gas Sci. Eng.* 21, 850–873. <https://doi.org/10.1016/j.jngse.2014.10.001>.
- Peng, J., Yin, Q., Li, G., et al., 2013a. The effect of actuator parameters on the critical flow velocity of a fluidic amplifier. *Appl. Math. Model.* 37 (14), 7741–7751. <https://doi.org/10.1016/j.apm.2013.03.011>.
- Peng, J., Zhang, Q., Li, G., et al., 2013b. Effect of geometric parameters of the bistable fluidic amplifier in the liquid-jet hammer on its threshold flow velocity. *Comput. Fluids* 82, 38–49. <https://doi.org/10.1016/j.compfluid.2013.05.002>.
- Pereira, G.C., De Souza, F.J., Martins, D.A.D.M., 2014. Numerical prediction of the erosion due to particles in elbows. *Powder Technol.* 261, 105–117. <https://doi.org/10.1016/j.jngse.2016.02.008>.
- Sarwar, W., Bergada, J.M., Mellibovsky, F., 2021. Onset of temporal dynamics within a low Reynolds-number laminar fluidic oscillator. *Appl. Math. Model.* 95, 219–235. <https://doi.org/10.1016/j.apm.2021.01.044>.
- Schultz, R.L., Connell, M.L., Ferguson, A.M., 2012. Vortex Controlled Variable Flow Resistance Device and Related Tools and Methods. US Patent, 2012/0292018 A1.
- Sedrez, T.A., Decker, R.K., Silva, M.K.D., et al., 2017. Experiments and CFD-based erosion modeling for gas-solids flow in cyclones. *Powder Technol.* 311, 120–131. <https://doi.org/10.1016/j.powtec.2016.12.059>.
- Shi, C., Luo, D., Zhu, X., 2022. Working characteristics of coiled tubing mechanical

- friction reducing tool based on Coanda effect. *J. Pet. Sci. Eng.* 212, 110223. <https://doi.org/10.1016/j.petrol.2022.110223>.
- Standen, R., Brunskill, D.G., 2012. Fluidic Impulse Generator. US Patent, 2012/0312156 A1.
- Tang, L., Zhang, S., Zhang, X., et al., 2021a. A review of axial vibration tool development and application for friction-reduction in extended reach wells. *J. Pet. Sci. Eng.* 199, 108348. <https://doi.org/10.1016/j.petrol.2021.108348>.
- Tang, L., Zhang, S., Zhang, X., et al., 2021b. Numerical investigation of the dynamic erosion behavior in fluidic oscillators with a periodic oscillating jet. *Powder Technol.* 395, 634–644.
- Tesař, V., 2008. Enhancing impinging jet heat or mass transfer by fluidically generated flow pulsation. *Chem. Eng. Res. Des.* 87, 181–192.
- Tesař, V., Hung, C., Zimmerman, W.B., 2006. No-moving-part hybrid-synthetic jet actuator. *Sensor Actuator Phys.* 125 (2), 159–169. <https://doi.org/10.1016/j.sna.2005.06.022>.
- Tesar, V., Jilek, M., 2013. Integral Fluidic Generator of Microbubbles. Colloquium Fluid Dynamics, Prague, Czech Republic, 2013.
- Tomac, M.N., Hossain, M.A., 2020. Flow and frequency characterization of the synchronized stacked sweeping jets. *AIAA J.* 59 (1). <https://doi.org/10.2514/1.j059643>.
- Woszidlo, R., Stumper, T., Nayeri, C., et al., 2014. Experimental study on bluff body drag reduction with fluidic oscillators. 52nd Aerospace Sciences Meeting.
- Wright, H.P., 1980. The Coanda meter—a fluidic digital gas flowmeter. *J. Phys. E Sci. Instrum.* 13 (4), 433.
- Zhang, X., Peng, J., Liu, H., et al., 2017. Performance analysis of a fluidic axial oscillation tool for friction reduction with the absence of a throttling plate. *Appl. Sci.-Basel* 7 (4), 360. <https://doi.org/10.3390/app7040360>.